EXTENDED PDF FORMAT
SPONSORED BY
Stem Cell Marker Antibodies
>Learn More
R&D SYSTEMS
www.rndsystems.com

Ancient Igneous Intrusions and Early Expansion of the Moon Revealed by GRAIL Gravity Gradiometry

Jeffrey C. Andrews-Hanna *et al.*

Science **339**, 675 (2013);
DOI: 10.1126/science.1231753

This copy is for your personal, non-commercial use only.

If you wish to distribute this article to others, you can order high-quality copies for your colleagues, clients, or customers by clicking here.

Permission to republish or repurpose articles or portions of articles can be obtained by following the guidelines here.

The following resources related to this article are available online at www.sciencemag.org (this information is current as of July 25, 2013):

Updated information and services, including high-resolution figures, can be found in the online version of this article at:
http://www.sciencemag.org/content/339/6120/675.full.html

Supporting Online Material can be found at:
http://www.sciencemag.org/content/suppl/2012/12/04/science.1231753.DC1.html

A list of selected additional articles on the Science Web sites **related to this article** can be found at:
http://www.sciencemag.org/content/339/6120/675.full.html#related

This article **cites 38 articles**, 7 of which can be accessed free:
http://www.sciencemag.org/content/339/6120/675.full.html#ref-list-1

This article has been **cited by** 3 articles hosted by HighWire Press; see:
http://www.sciencemag.org/content/339/6120/675.full.html#related-urls

This article appears in the following **subject collections:**
Planetary Science
http://www.sciencemag.org/cgi/collection/planet_sci

Downloaded from www.sciencemag.org on July 25, 2013

Science (print ISSN 0036-8075; online ISSN 1095-9203) is published weekly, except the last week in December, by the American Association for the Advancement of Science, 1200 New York Avenue NW, Washington, DC 20005. Copyright 2013 by the American Association for the Advancement of Science; all rights reserved. The title *Science* is a registered trademark of AAAS.

31. S. Mueller, G. J. Taylor, R. J. Phillips, *J. Geophys. Res.* **93** (B6), 6338 (1988).
32. A. Khan, J. A. D. Connolly, J. Maclennan, K. Mosegaard, *Geophys. J. Int.* **168**, 243 (2007).
33. O. L. Kuskov, V. A. Kronrod, *Phys. Earth Planet. Inter.* **107**, 285 (1998).
34. S. M. Clifford, *J. Geophys. Res.* **98** (E6), 10973 (1993).
35. S. Schumacher, D. Breuer, *J. Geophys. Res.* **111** (E2), E02006 (2006).

Acknowledgments: The GRAIL mission is supported by the Discovery Program of NASA and is performed under contract to the Massachusetts Institute of Technology and the Jet Propulsion Laboratory, California Institute of Technology. Additional support for this work was provided by the French Space Agency (CNES), the Centre National de la Recherche Scientifique, and the UnivEarthS LabEx project of Sorbonne Paris Cité. Data products will be made available from the authors upon request.

Supplementary Materials
www.sciencemag.org/cgi/content/full/science.1231530/DC1
Supplementary Text
Figs. S1 to S13
Table S1
References (*36*–*73*)

15 October 2012; accepted 27 November 2012
Published online 5 December 2012;
10.1126/science.1231530

Ancient Igneous Intrusions and Early Expansion of the Moon Revealed by GRAIL Gravity Gradiometry

Jeffrey C. Andrews-Hanna,[1]* Sami W. Asmar,[2] James W. Head III,[3] Walter S. Kiefer,[4] Alexander S. Konopliv,[2] Frank G. Lemoine,[5] Isamu Matsuyama,[6] Erwan Mazarico,[5,7] Patrick J. McGovern,[4] H. Jay Melosh,[8] Gregory A. Neumann,[5] Francis Nimmo,[9] Roger J. Phillips,[10] David E. Smith,[7] Sean C. Solomon,[11,12] G. Jeffrey Taylor,[13] Mark A. Wieczorek,[14] James G. Williams,[2] Maria T. Zuber[7]

The earliest history of the Moon is poorly preserved in the surface geologic record due to the high flux of impactors, but aspects of that history may be preserved in subsurface structures. Application of gravity gradiometry to observations by the Gravity Recovery and Interior Laboratory (GRAIL) mission results in the identification of a population of linear gravity anomalies with lengths of hundreds of kilometers. Inversion of the gravity anomalies indicates elongated positive-density anomalies that are interpreted to be ancient vertical tabular intrusions or dikes formed by magmatism in combination with extension of the lithosphere. Crosscutting relationships support a pre-Nectarian to Nectarian age, preceding the end of the heavy bombardment of the Moon. The distribution, orientation, and dimensions of the intrusions indicate a globally isotropic extensional stress state arising from an increase in the Moon's radius by 0.6 to 4.9 kilometers early in lunar history, consistent with predictions of thermal models.

Planetary gravity analyses have been limited historically to large-scale features associated with high contrasts in density, due to the low resolution and low signal-to-noise ratio of the data. As a result, small-scale subsurface structures such as faults and dikes that have been inferred from their surface expressions have not been resolved in the gravity field, and structures lacking a direct surface manifestation have been largely undocumented. This situation has posed a challenge for studies of the early evolution of the Moon, because the near saturation of the surface by impact craters has erased much of the geological record from the first ~700 million years (My) of lunar history (*1*), spanning the critical period of time between the solidification of the lunar magma ocean and the end of major impact basin formation ~3.8 billion years ago (Ga) (*2*). Data from the Gravity Recovery and Interior Laboratory (GRAIL) mission (*3*) now permit the expansion of the gravity field to spherical harmonic degree and order 420 (model GL0420A), corresponding to a half-wavelength resolution of ~13 km at the lunar surface (*4*). This resolution is sufficient to resolve short-wavelength density anomalies, such as intrusions that have a higher density than the surrounding rocks and faults that offset layers of differing density.

Here, we apply the technique of gravity gradiometry to the GRAIL gravity field, using the second spatial derivatives of the gravitational potential to highlight short-wavelength features associated with discrete structures (*5*). In terrestrial applications, gradients are typically measured directly by a three-axis gradiometer on an aerial or satellite-borne platform (*5*, *6*), but in our work, we calculated the gradients from the potential field. To emphasize subsurface structures, we used gradients of the Bouguer potential (calculated as the difference between the measured gravitational potential and the potential arising from the effects of topography) (*4*). We then calculated the maximum amplitude of the second horizontal derivative of the Bouguer potential at each point on the surface [Γ_{hh}, measured in Eötvös units (E), where $1E = 10^{-9}$ s^{-2} (*7*)]. The resulting horizontal Bouguer gradient map (Fig. 1) displays a rich array of short-wavelength structures in the lunar crust.

The dominant features in the gradient map are the ring structures surrounding the large impact basins. These rings are also observed in the Bouguer gravity (Fig. 1A) (*4*), but they are resolved in the gradient map as discrete structures. Outside of the basins, a large number of irregular small-scale anomalies are observed with typical values of $\pm 10E$, probably arising from small-scale density anomalies in the upper crust associated with variations in composition or porosity. In addition, a number of elongated linear gravity anomalies (LGAs) characterized by negative gradients stand out clearly above the background variability. Four of the LGAs have lengths exceeding 500 km (Fig. 2). These anomalies closely follow linear paths (great circles) across the surface to within root mean square deviations of 1 to 3% of their lengths. Inspection of the most distinct LGAs yields 22 probable anomalies with a combined length of 5300 km and an additional 44 possible anomalies with a combined length of 8160 km for a total length of 13,460 km (Fig. 1C). An independent automated algorithm identified 46 anomalies with a combined length of 10,600 km (*7*). Such markedly linear structures in natural geologic systems are typically associated with faults or dikes. Averaged profiles of the Bouguer gravity anomaly perpendicular to the lineations show these structures to be associated with narrow positive-gravity anomalies (Fig. 3), indicating subsurface structures of increased density consistent with the interpretation that the features are mafic igneous intrusions.

We used a Monte Carlo approach to invert the average Bouguer gravity profiles across the LGAs for the physical properties of the subsurface density anomalies, treating them as tabular bodies of unknown top depth, bottom depth, width, and density contrast (*7*). A continuous set of solutions exists with comparable misfits to the data, as a result of the fundamental nonuniqueness of potential field data with respect

[1]Department of Geophysics and Center for Space Resources, Colorado School of Mines, Golden, CO 80401, USA. [2]Jet Propulsion Laboratory, Pasadena, CA 91109, USA. [3]Department of Geological Sciences, Brown University, Providence, RI 02912, USA. [4]Lunar and Planetary Institute, Houston, TX 77058, USA. [5]Solar System Exploration Division, NASA Goddard Space Flight Center, Greenbelt, MD 20771, USA. [6]Lunar and Planetary Laboratory, University of Arizona, Tucson, AZ 85721, USA. [7]Department of Earth, Atmospheric and Planetary Sciences, Massachusetts Institute of Technology, Cambridge, MA 02139–4307, USA. [8]Department of Earth and Atmospheric Sciences, Purdue University, West Lafayette, IN 47907, USA. [9]Department of Earth and Planetary Sciences, University of California, Santa Cruz, Santa Cruz, CA 95064, USA. [10]Planetary Science Directorate, Southwest Research Institute, Boulder, CO 80302, USA. [11]Department of Terrestrial Magnetism, Carnegie Institution of Washington, Washington, DC 20015, USA. [12]Lamont-Doherty Earth Observatory, Columbia University, Palisades, NY 10964, USA. [13]Hawaii Institute of Geophysics and Planetology, University of Hawaii, Honolulu, HI 96822, USA. [14]Institut de Physique du Globe de Paris, Sorbonne Paris Cité, Université Paris Diderot, Case 7071, Lamarck A, 5, rue Thomas Mann, 75205 Paris Cedex 13, France.

*To whom correspondence should be addressed. E-mail: jcahanna@mines.edu

Downloaded from www.sciencemag.org on July 25, 2013

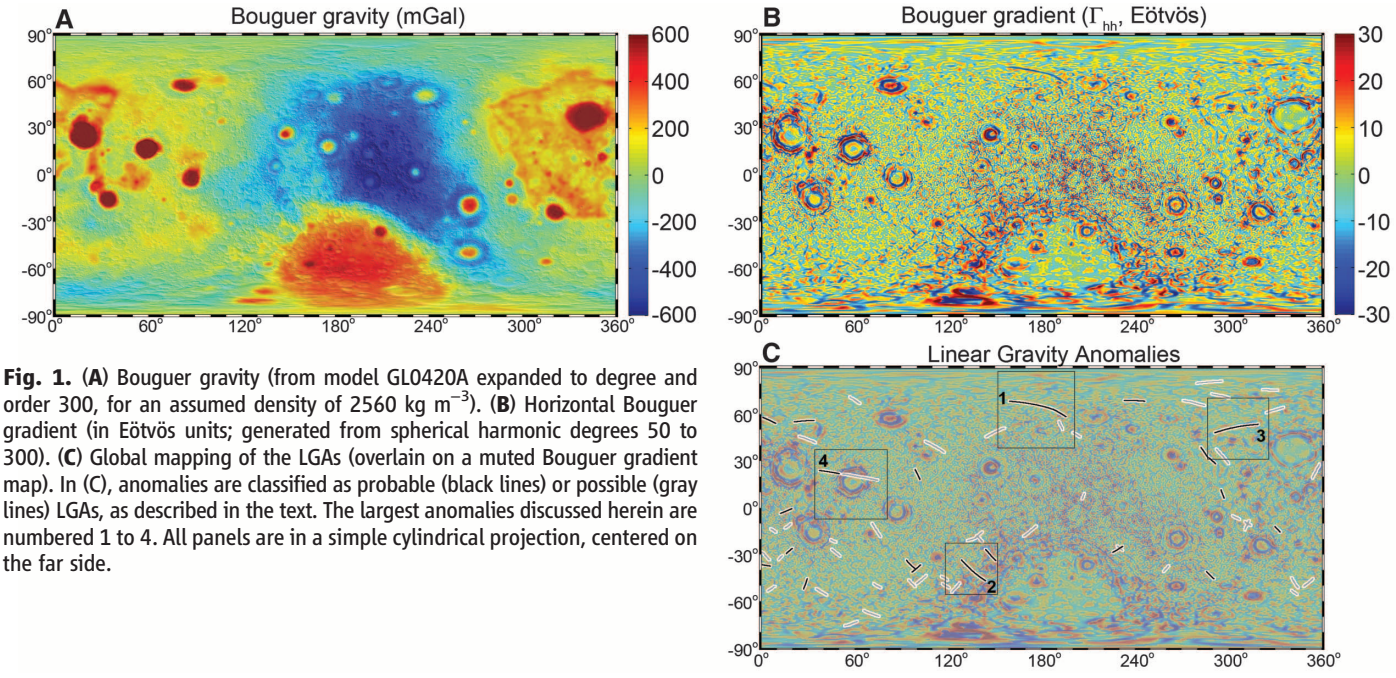

Fig. 1. (**A**) Bouguer gravity (from model GL0420A expanded to degree and order 300, for an assumed density of 2560 kg m^{-3}). (**B**) Horizontal Bouguer gradient (in Eötvös units; generated from spherical harmonic degrees 50 to 300). (**C**) Global mapping of the LGAs (overlain on a muted Bouguer gradient map). In (C), anomalies are classified as probable (black lines) or possible (gray lines) LGAs, as described in the text. The largest anomalies discussed herein are numbered 1 to 4. All panels are in a simple cylindrical projection, centered on the far side.

to subsurface structures. From the variability in the gravity profiles, we also determined the 95% confidence intervals of the model parameters. For one of the best-defined anomalies (LGA-1) (Fig. 2A), the best-fit solutions have density contrasts of 160 to 960 kg m^{-3} in bodies with widths of 5 to 25 km extending between a top depth of 10 to 15 km and a bottom depth of 76 to 91 km (Fig. 3 and Table 1). The top depth may correspond to either the top of the intrusion or the maximum depth of impact brecciation and gardening, above which the density contrast would become less distinct. Similarly, the bottom depth may correspond to either the base of the intrusion or the depth of the crust-mantle interface, below which the density contrast between the intrusion and the host rocks would decrease markedly. For LGA-2, a shallow top depth is suggested by the observation that the 116-km–diameter impact crater Roche, excavating the crust to a depth of ~7 km and brecciating it to greater depths, results in a modest reduction in the magnitude of the anomaly, whereas smaller craters have no effect (Fig. 2).

The dimensions of the anomaly sources can be further constrained with the use of independent constraints on the density contrast. The mean density of the upper crust derived from GRAIL is 2550 ± 250 kg m^{-3} (*8*). Although the composition of the intrusions is unknown, representative values can be taken from the measured densities of lunar igneous rocks of 3100 to 3350 kg m^{-3} (*9*), yielding density contrasts of 550 to 860 kg m^{-3}. For density contrasts of 550 and 800 kg m^{-3}, the best-fit solutions for LGA-1 collapse to a point in parameter space, with widths of 7.6 and 5.3 km, respectively (Table 1). However, the bottom depth (85 to 86 km) for these solutions is probably deeper than the base of the crust, below which the reduced density contrast would contribute little to the observed gravity. If the base of the density anomaly is constrained to be 40 km, comparable to the mean crustal thickness (*8*), the best-fit widths for density contrasts of 550 and 800 kg m^{-3} increase to 29.1 and 23.5 km, with top depths of 24.9 and 26.9 km. A bottom depth of 60 km results in widths of 11.9 and 8.3 km and top depths of 19.0 and 19.4 km. Similar results are found from the inversions of LGAs 2 and 4, with a total range of best-fit widths of 5 to 12 km for density contrasts of 550 and 800 kg m^{-3} with the bottom depth unconstrained or 7 to 41 km for bottom depths of 40 to 60 km (*7*). LGA-3 requires a greater width of 13 to 18 km or 49 to 82 km with the bottom depth constrained to 40 to 60 km, in keeping with the greater width of the gravity anomaly.

Although the lengths and linearity of the density anomalies are similar to those of giant dike swarms on Earth, Mars, and Venus, their widths greatly exceed typical dike widths of tens of meters (*10*, *11*). Vertical tabular intrusions with aspect ratios similar to those proposed here can form by diapirism when the viscosity contrast between the magma and host rock is in the range of 10^6 to 10^8 (*12*). For mafic intrusions, this low viscosity contrast would require either a partially crystalline intrusion or a highly ductile or partially molten host rock. The source of the gravity anomalies may be analogous to the Great Dyke of Zimbabwe, which probably formed as a result of shallow intrusive activity during ancient rifting (*13*). This elongated layered ultramafic intrusion measures 550 km in length, 3 to 11 km in width, and up to 12 km in vertical extent (*13*, *14*). Intrusive bodies of similar scale have been inferred to exist beneath the Valles Marineris region of Mars on the basis of collapse features (*15*), formed in response to lithospheric extension and intrusion (*16*). Alternatively, narrow swarms of closely spaced dikes (*17*) can match the gravity anomalies but would require tens to hundreds of dikes confined within zones less than ~40 km wide that extend over distances of hundreds of kilometers. Similar narrow dike swarms with lengths up to 100 km form above elongated axial magma chambers in rifts on Earth (*18*). A combination of the above processes may be responsible for the anomalies, with a single vertical tabular intrusion forming in a partially molten lower crust, sourcing a swarm of closely spaced dikes in the more brittle upper crust. The large bottom depths from the inversions permit the intrusions to extend into the mantle, as would be required if the rise of magma were governed by neutral buoyancy (*19*). Although the specific nature and formation mechanism of the intrusions remains uncertain, some form of intrusive activity in a horizontally extensional stress regime is indicated by all of the analogous structures.

Lunar dikes previously inferred from geological analyses (*20*) are not detected in the gravity data. This result is not surprising, because isolated dikes with widths of up to tens of meters would have gravity anomalies two orders of magnitude smaller than these LGAs. A linear magnetic anomaly interpreted as a dense swarm of dikes on the floor of the South Pole–Aitken basin (*17*) is not evident in the gravity gradients but is associated with a broad positive Bouguer gravity anomaly where it extends outside of the basin (*7*). This anomaly may be consistent with a dense dike swarm, with the lower-density contrast relative to the mafic crust in the floor of the basin possibly accounting for the nondetection there. Alternatively, the poor expression of the magnetic anomalies in the gravity data may

Downloaded from www.sciencemag.org on July 25, 2013

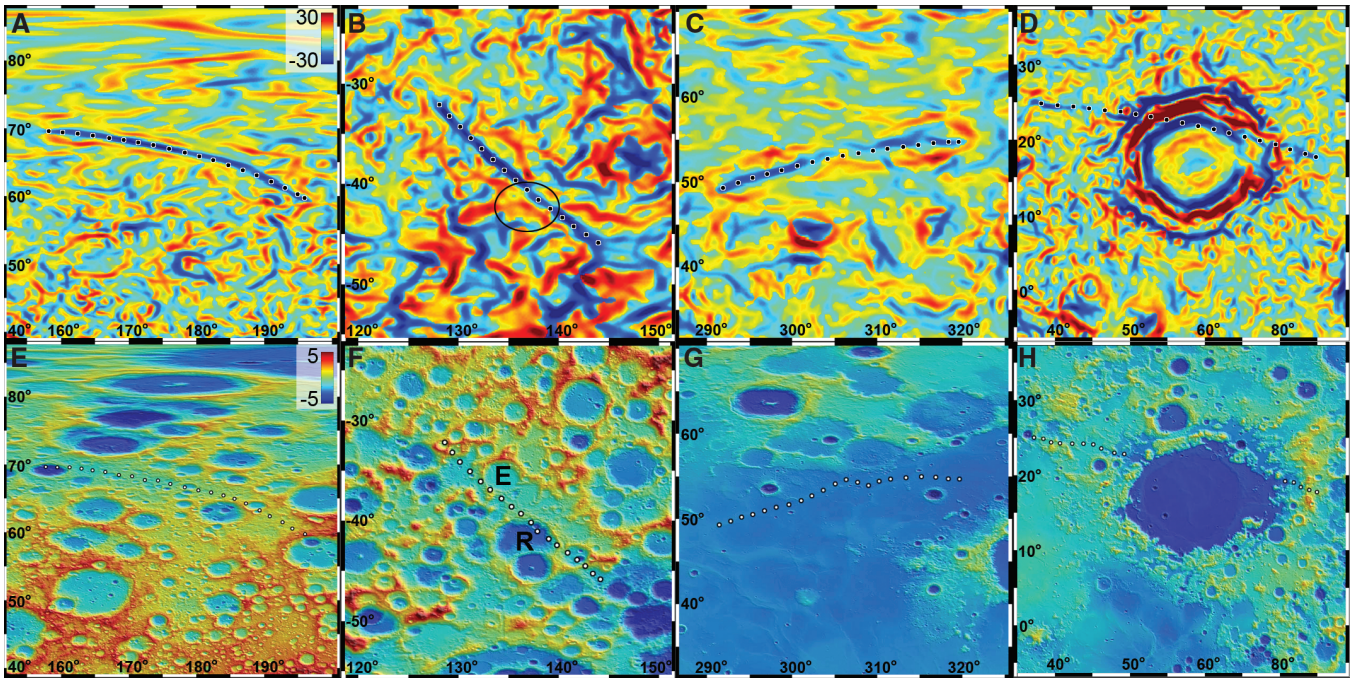

Fig. 2. (**A** to **D**) Horizontal Bouguer gradient (in Eötvös units) and (**E** to **H**) topography (in kilometers) in the vicinity of four prominent LGAs (LGAs 1 to 4 are shown in order from left to right; see Fig. 1 for context). The dots in the upper panels follow great-circle fits to the anomalies, whereas the dots in the lower panels follow the paths of the anomalies themselves. The craters Eötvös (E) and Roche (R) are labeled in (F), and Roche is outlined in (B); the gravity gradient shows reduced amplitude within the latter crater.

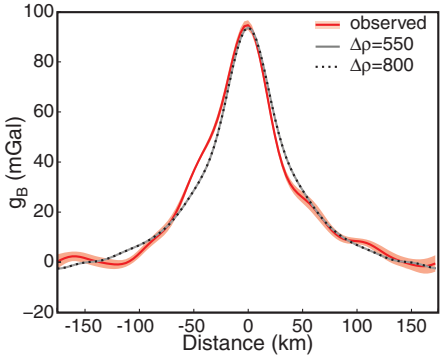

Fig. 3. Mean profile and ±f1 standard error range (in red and pink, respectively) of the Bouguer gravity anomaly (g_B) over LGA-1. The predicted gravity anomalies from the best-fit vertical tabular intrusions for density contrasts ($\Delta\rho$) of 550 and 800 kg m^{-3} are shown for comparison (overlapping gray and dashed black lines, respectively).

Table 1. Density contrast ($\Delta\rho$), width (w), top depth (z_{top}), and bottom depth (z_{bot}) from the inversion of LGA-1, including the best-fit range in parameters and the 95% confidence intervals (C.I.) for the full inversion (*7*) and the best-fit (±95% C.I. range) solutions for assumed density contrasts of 550 and 800 kg m^{-3}.

	Best fit	95% C.I.	Δρ = 550	Δρ = 800
$\Delta\rho$ (kg m^{-3})	160–960	90–940	550	800
w (km)	4.5–24.9	5.7–46.7	$7.6^{+35.2}_{-1.4}$	$5.3^{+34.2}_{-0.9}$
z_{top} (km)	10.3–14.8	6.0–38.8	$13.0^{+28.2}_{-5.2}$	$13.3^{+30.0}_{-4.3}$
z_{bot} (km)	75.6–90.6	30–96	86^{+10}_{-55}	85^{+9}_{-56}

support Fe-rich material derived from the basin-forming projectile as the source of the magnetic anomalies (*21*).

Averaged magnetic (*22*) and topographic (*23*) profiles across the LGAs generally reveal no correlation of either data set with the gravity anomalies (*7*). Forward models of the expected magnetic anomalies require that any magnetization be substantially less than 0.1 A/m for most of the lineations, indicating that the intrusions either have very low magnetic susceptibility or cooled in the absence of an external field. A topographic signature associated with the intrusions might be expected as a result of tectonic uplift, flexural subsidence, graben formation (*24*), or collapse of the surface into the magma chambers (*15*), yet none is observed. A number of LGAs are located in crater-saturated areas (Fig. 2) and lack any obvious surface expression in topography, image, or other remote sensing data sets. The absence of a surface expression is consistent with an age for the structures that predates the superimposed crater population and the surface geologic record.

The age of the structures can be further constrained by crosscutting relationships. Several linear anomalies are observed radial to the South Pole–Aitken impact basin, which is the oldest basin on the Moon. This radial orientation indicates that the formation of these structures was influenced by the preexisting basin. The lack of a surface signature rules out an origin as rays of dense impact ejecta (*7*). A 1000-km-long anomaly (LGA-4) crosses the Crisium basin at an oblique angle (Fig. 2), but no trace of the anomaly is found within the basin itself. This geometry suggests that this anomaly predated Crisium and that the underlying structure was destroyed within the basin cavity by the impact. This timing is supported by the fact that the intrusion was not deflected by the strong flexural stresses associated with the pre-mare mascon (*25*) and later mare load within the basin. By these arguments, the South Pole–Aitken and Crisium basins place the formation of the largest intrusions within the pre-Nectarian to early Nectarian time frame, before the end of the basin-forming epoch at ~3.8 Ga. This age is consistent with the lunar intrusive activity between 4.2 and 4.5 Ga that was responsible for the formation of the plutonic Mg-suite rocks (*26*), though it is not possible to directly link these intrusions to any particular rock type with the use of gravity data alone.

Tabular igneous intrusions form perpendicular to the most extensional principal stress direction (*27*), leading to the formation of vertical dikes in a horizontally extensional stress field and sills in a horizontally compressional stress field.

Downloaded from www.sciencemag.org on July 25, 2013

Although local flexural stresses or structural control can alter the orientations of intrusions (*7*), the LGAs are distributed uniformly across the Moon and show no clear preferred orientations or association with known flexurally supported loads. This pattern indicates largely isotropic horizontal extension, as would be expected to arise from global expansion. However, the lunar lithosphere is thought to have been in a state of compression throughout most of its history as a result of interior cooling and global contraction (*28*). Superimposed stresses associated with the outward migration of the Moon, with or without contemporaneous true polar wander, are similarly inconsistent with the locations and orientations of the LGAs (*7*, *29*). At the time of the intrusive activity inferred here, the lithosphere must have been in a horizontally extensional stress state to accommodate the inflation of the vertical tabular intrusions. Taking the total length of the probable intrusion population of 5300 km and the typical best-fit widths of 5 to 40 km, the resulting horizontal extensional strain of 0.035 to 0.27% equates to an increase in the lunar radius by 0.6 to 4.8 km. However, this estimate is complicated by the possibility of viscous accommodation of some of the growth of the intrusions or lithospheric extension not accompanied by intrusive activity that would go undetected by GRAIL.

Such a period of early extension was predicted by some thermal history models (*28*), developed to account for the absence of a global population of large thrust faults on the Moon similar to those found on Mercury. The thermal models best matched that constraint with an initial condition that included a 200- to 300-km-deep magma ocean and a cooler deep interior, leading to coupled warming of the interior and cooling of the outer shell, with net expansion in the first billion years followed by modest global contraction. Cooling and contraction of the lunar lithosphere could also have contributed to extensional strain at the depths of these intrusions within the first few tens of millions of years after lunar crustal formation. This thermal inversion may be a natural outcome of the post-accretional temperature profile of the Moon (*30*). Thermal history models that satisfy the constraint of <1 km decrease in radius over the past 3.8 billion years (Gy) also predict 2.7 to 3.7 km of global expansion during the first ~1 Gy, with the highest rates occurring during the first 0.5 Gy (*28*), consistent with our proposed period of expansion. The amount of predicted expansion is sensitive to the depth of the magma ocean and the initial temperature of the deep interior. However, no direct geological evidence for this early expansion has previously been found, as a consequence of the intense cratering of the surface at that time. This earliest epoch of lunar expansion is now revealed by GRAIL gravity data, which allows us to see through the surface geology to the hidden structures beneath. This result places a constraint on lunar evolution and raises important questions regarding the early evolution of other terrestrial planets, because the first ~700 My of planetary evolution is poorly preserved in the geological records of all planets.

References and Notes

1. W. K. Hartmann, R. W. Gaskell, *Meteoritics* **32**, 109 (1997).
2. D. Stöffler, G. Ryder, *Space Sci. Rev.* **96**, 9 (2001).
3. M. T. Zuber *et al.*, *Space Sci. Rev.* 10.1007/s11214-012-9952-7 (2013).
4. M. T. Zuber *et al.*, *Science* **339**, 668 (2013).
5. C. Jekeli, *Surv. Geophys.* **27**, 257 (2006).
6. R. Rummel, W. Yi, C. Stummer, *J. Geod.* **85**, 777 (2011).
7. Materials and methods are available as supplementary materials on *Science* Online.
8. M. A. Wieczorek *et al.*, *Science* **339**, 671 (2013).
9. W. S. Kiefer, R. J. Macke, D. T. Britt, A. J. Irving, G. J. Consolmagno, *Geophys. Res. Lett.* **39**, L07201 (2012).
10. R. E. Ernst, E. B. Grosfils, D. Mège, *Annu. Rev. Earth Planet. Sci.* **29**, 489 (2001).
11. L. Wilson, J. W. Head III, *Lunar Planet. Sci.* **40**, abstract 1160 (2009).
12. A. M. Rubin, *Earth Planet. Sci. Lett.* **119**, 641 (1993).
13. A. H. Wilson, *J. Petrol.* **23**, 240 (1982).
14. F. Podmore, A. H. Wilson, "A reappraisal of the structure and emplacement of the Great Dyke, Zimbabwe," *Geol. Assoc. Canada Special Paper 33* (1985), pp. 317–330.
15. D. Mège, A. C. Cook, E. Garel, Y. Lagabrielle, M. Cormier, *J. Geophys. Res.* **108**, 5044 (2003).
16. J. C. Andrews-Hanna, *J. Geophys. Res.* **117**, E04009 (2012).
17. M. E. Purucker, J. W. Head III, L. Wilson, *J. Geophys. Res.* **117**, E05001 (2012).
18. A. Gudmundsson, *J. Volcanol. Geotherm. Res.* **64**, 1 (1995).
19. J. W. Head III, L. Wilson, *Geophys. Res. Lett.* **18**, 2121 (1991).
20. J. W. Head III, L. Wilson, *Planet. Space Sci.* **41**, 719 (1993).
21. M. A. Wieczorek, B. P. Weiss, S. T. Stewart, *Science* **335**, 1212 (2012).
22. M. E. Purucker, J. B. Nicholas, *J. Geophys. Res.* **115**, E12007 (2010).
23. D. E. Smith *et al.*, *Geophys. Res. Lett.* **37**, L18204 (2010).
24. A. M. Rubin, *J. Geophys. Res.* **97**, 1839 (1992).
25. J. C. Andrews-Hanna, *Icarus* **222**, 159 (2013).
26. G. A. Snyder, C. R. Neal, L. A. Taylor, A. N. Halliday, *J. Geophys. Res.* **100**, 9365 (1995).
27. E. M. Anderson, *The Dynamics of Faulting and Dyke Formation with Application to Britain* (Oliver and Boyd, London, ed. 2, 1951).
28. S. C. Solomon, *Phys. Earth Planet. Inter.* **15**, 135 (1977).
29. H. J. Melosh, *Icarus* **43**, 334 (1980).
30. W. M. Kaula, *J. Geophys. Res.* **84**, 999 (1979).

Acknowledgments: The GRAIL mission is a component of the NASA Discovery Program and is performed under contract to the Massachusetts Institute of Technology and the Jet Propulsion Laboratory. J.C.A.-H., J.W.H., W.S.K., I.M., P.J.M., F.N., and G.J.T. were supported by grants from the NASA GRAIL Guest Scientist Program. The data used in this study will have been archived in the Geosciences Node of the NASA Planetary Data System by the time of publication.

Supplementary Materials

www.sciencemag.org/cgi/content/full/science.1231753/DC1
Materials and Methods
Supplementary Text
Figs. S1 to S13
Tables S1 to S6
References (*31*–*47*)

19 October 2012; accepted 27 November 2012
Published online 5 December 2012;
10.1126/science.1231753

Proton Donor Acidity Controls Selectivity in Nonaromatic Nitrogen Heterocycle Synthesis

Simon Duttwyler,[1] Shuming Chen,[1] Michael K. Takase,[1] Kenneth B. Wiberg,[1] Robert G. Bergman,[2] Jonathan A. Ellman[1]*

Piperidines are prevalent in natural products and pharmaceutical agents and are important synthetic targets for drug discovery and development. We report on a methodology that provides highly substituted piperidine derivatives with regiochemistry selectively tunable by varying the strength of acid used in the reaction. Readily available starting materials are first converted to dihydropyridines via a cascade reaction initiated by rhodium-catalyzed carbon-hydrogen bond activation. Subsequent divergent regio- and diastereoselective protonation of the dihydropyridines under either kinetic or thermodynamic control provides two distinct iminium ion intermediates that then undergo highly diastereoselective nucleophilic additions. X-ray structural characterization of both the kinetically and thermodynamically favored iminium ions along with density functional theory calculations provide a theoretical underpinning for the high selectivities achieved for the reaction sequences.

Piperidines are saturated, nonplanar nitrogen heterocycles upon which the display of functionality has provided some of the most well-known pharmaceuticals, as exemplified by traditional drugs such as quinine, morphine (and its many synthetic analogs such as oxycodone), as well as a number of more recent blockbusters, including plavix for the treatment of stroke, cialis for erectile dysfunction, and aricept for Alzheimer's treatment (Fig. 1A) (*1*). The physical properties and therapeutic importance of the piperidine scaffold are consistent with recent retrospective analyses of drug-discovery research suggesting that renewed emphasis should be placed on the preparation, evaluation, and development of compounds with

Downloaded from www.sciencemag.org on July 25, 2013